Acta Materialia 274 (2024) 120027

Contents lists available at ScienceDirect

Acta Materialia

journal homepage: www.elsevier.com/locate/actamat

Growth-associated emergence of spontaneous magnetization in Al-doped Cr_2O_3 thin film

Tatsuo Tada [a,1], Hiroki Sakurai [a,2], Kentaro Toyoki [a,b,c], Satoshi Ichikawa [d], Toshiaki Ina [e], Noriaki Kishida [a], Yoshinori Kotani [e], Masashi Nakamoto [a], Kota Mori [a], Ryoichi Nakatani [a,b,c], Yu Shiratsuchi [a,b,c,*]

[a] Graduate School of Engineering, Osaka University, Suita, Osaka 565-0871, Japan
[b] Institute for Open and Transdisciplinary Research Initiatives, Osaka University, Suita, Osaka 565-0871, Japan
[c] Center for Spintronics Research Network, Osaka University, Toyonaka, Osaka 560-8531, Japan
[d] Research Center for Ultra-High Voltage Electron Microscopy, Osaka University, Ibaraki, Osaka 567-0047, Japan
[e] Japan Synchrotron Radiation Research Institute (JASRI/SPring-8), Sayo, Hyogo 679-5198, Japan

ARTICLE INFO

Keywords:
Antiferromagnet
Ferrimagnet
Cr_2O_3
Epitaxial growth
Spintronics

ABSTRACT

Development of antiferromagnetic/ferrimagnetic materials has been an area of active pursuit to advance the antiferromagnetic/ferrimagnetic spintronics. In this paper, we investigated the emergence of the spontaneous magnetization M_S in the antiferromagnetic Cr_2O_3 thin film by the Al substitution. In the case of the $(Cr_{1-x}Al_x)_2O_3(0001)$ thin films, M_S increases with increasing Al composition x up to $x \sim 0.21$. The magnitude of M_S decreases abruptly for $x > 0.22$, accompanied with the collapse of the crystal formation. We found that the induction of the spontaneous magnetization was highly associated with the growth process. The magnitude of M_S depends on the growth direction of the film: M_S at 10 K for $x = 0.13 \pm 0.01$ is 80 kA/m, 30 kA/m and 0 kA/m for (0001), $(01\bar{1}2)$ and $(11\bar{2}0)$ films, respectively. The difference in M_S with the growth direction is relevant to the magnetic sublattice selective substitution of Al during the thin film growth. This specific substitution occurs in the growth plane having the layer-by-layer stacking of the magnetic sublattice, which was verified by the direct observations using the scanning transmission electron microscope.

1. Introduction

Ferrimagnets are a kind of magnetic materials, and they show the weak but finite spontaneous magnetization due to the unbalance of antiparallelly coupled sublattice magnetic moments, e.g, $|\mathbf{m}_1| \neq |\mathbf{m}_2|$, $\angle(\mathbf{m}_1, \mathbf{m}_2) = \pi$ (Fig. 1(a)). The ferrimagnets offer the combined benefits of ferromagnets and antiferromagnets; the easy control and detection of magnetic order parameter by an external field due to the Zeeman coupling and the antiferromagnetic (AFM)-like ultrafast dynamics due to the antiparallel exchange-coupling between neighboring magnetic moments [1-7]. Especially, the former characteristic solves the problem in the AFM materials wherein the magnetic moments are fully canceled within the unit cell, e.g, $|\mathbf{m}_1| = |\mathbf{m}_2|$, $\angle(\mathbf{m}_1, \mathbf{m}_2) = \pi$ (Fig. 1(b)). This benefit makes the ferrimagnets to be an alternative material platform of the emerging AFM spintronics [8]. To date, the rare earth-transition metal (RE-TM) based ferrimagnets such as Gd-(Fe-)Co [9-14] and Tb-(Fe-)Co [15-17] are widely explored. In these materials, the finite spin polarization makes it possible to polarize and detect the spin currents, which advances the current-driven ferrimagnetic spintronics [8,9,12,15,18,19]. For instance, the ultrafast domain wall velocity exceeding 1000 m/s was achieved [18,19] as a consequence of the compensation of the angular momentum with surviving the net magnetization.

In the current-driven spintronics, the huge current density typically exceeding 10^{11} A/m^2 [12] is required to control the magnetic moments and it gives rise to the large joule heating and the high-power consumption. The voltage-driven spintronics is a counterpart, and it can reduce the operation power due to no need of the electric current. However, since a voltage (an electric field E) is unconjugated with a magnetic moment, the elaborated path connecting magnetism with E is required. The magnetoelectric (ME) effect [20-23], an interplay between

* Corresponding author at: Graduate School of Engineering, Osaka University, Suita, Osaka 565-0871, Japan.
E-mail address: shiratsuchi@mat.eng.osaka-u.ac.jp (Y. Shiratsuchi).
[1] (TT) contributed equally to this work.
[2] (HS) contributed equally to this work.

https://doi.org/10.1016/j.actamat.2024.120027
Received 24 January 2024; Received in revised form 30 April 2024; Accepted 20 May 2024
Available online 20 May 2024

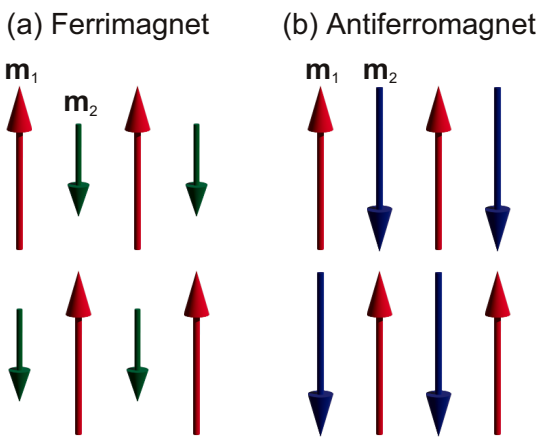

Fig. 1. Schematic drawing of the typical arrangement of magnetic moments in (a) ferrimagnet and (b) antiferromagnet.

magnetism and dielectricity, is a possible route to manage the magnetic moment via *E*. Since the net magnetization is not required for the ME effect to occur, the ME mechanism is applicable to the pure antiferromagnets. Cr_2O_3 is a prototypical ME material exhibiting the antiferromagnetism [20-24]. It has been so far demonstrated the ME-driven 180° switching of the Nèel vector $\mathbf{l}$ ($= \mathbf{m}_1 - \mathbf{m}_2$) using the bulk Cr_2O_3 [25,26] and Cr_2O_3 thin film [27-30]. In most of previous reports [25-31], the interfacial exchange coupling with the ferromagnetic (FM) layer, typically Co is used to complement the difficulty to detect $\mathbf{l}$ in Cr_2O_3. This scheme, however, yields the excess energy barrier for the switching of $\mathbf{l}$ [32-34]. The induction of the weak but finite spontaneous magnetization, e.g. the ferrimagnetic ME insulator is helpful for the low-energy operation [35] via the finite Zeeman coupling with the external magnetic field. Although there are conventional and typical ferrimagnetic insulators such as Fe_3O_4 [36-38] and $Y_3Fe_5O_{12}$ [39-41], the ME-mechanism is not applicable to these materials because these are not in the category of the ME materials. Since the spatial- and time-inversion symmetry breakings are required for the materials to take the ME characteristics [20,42], the straightforward way to create ferrimagnetic ME materials is to dope other elements in the ME-AFM materials in maintaining the crystal structure with the spatial inversion symmetry. It has been so far reported that the Al and Ir doping into the Cr_2O_3(0001) thin film induced the finite magnetization [43,44] and that the film maintained the ME ability [43]. In the previous reports, the ME effect in the doped film was observed for the low dopant concentration, e.g., <3.7at% [43], and the high dopant concentration would deteriorate the ME coupling strength. Since the ME effect is strongly relevant to the ligand field acting on the magnetic elements and the detailed understanding on the local structure around the magnetic elements is essential for the deep understanding and further development of a class of the ME ferrimagnetic insulator. Although the site-selective substitution [43] and the boundary magnetization in conjunction with the ME effect [44] have been discussed as the origin of the spontaneous magnetization, the in-depth investigation on the crystal structure is lacked, which veils the detailed mechanism of the induced spontaneous magnetization. In this paper, we report the emergence of the finite spontaneous magnetization in the Al-doped Cr_2O_3 thin films in collaboration with the in-depth structural investigation. It is found that the emergence of the spontaneous magnetization is associated with the formation of Cr_2O_3 crystal, e.g., not amorphous, and it is also highly relevant to the thin film growth process. Our thorough exploration reveal that the spontaneous magnetization is caused by the magnetic sublattice-selective substitution of non-magnetic Al, and this specific substitution occurs during the thin film growth along the direction having the layer-by-layer stacking structure of the magnetic sublattice.

2. Experimental

The Al-doped Cr_2O_3 thin films with the Al composition *x*, $(Cr_{1-x}Al_x)_2O_3$ films were grown on the α-Al_2O_3 substrate by using the reactive DC magnetron sputtering method. The base pressure of the deposition chamber was below 1×10^{-6} Pa. The film thickness was designed as 200 nm for all studied films except for the special note. The deposition temperature was 773 K. We employed three types of the substrate having the different orientation: (0001), $(01\bar{1}2)$ and $(11\bar{2}0)$. The α-Al_2O_3(0001) substrate was mainly used and other two were used in the final part of this paper. The metallic Cr and Al targets were co-sputtered using Ar and O_2 gas mixture. The *x* value was varied by changing the input power of Al target in maintaining the input power of the Cr target. The actual value of *x* was measured by the wave-length dispersed X-ray fluorescence (XRF) measurements. The XRF measurements was done using the films grown on the Mo foil which was simultaneously prepared together with the main films by locating the Mo foil aside the α-Al_2O_3 substrate.

Magnetic properties were characterized based on the magnetization measurements using a superconducting quantum interference device (SQUID) magnetometer (MPMS5T, Quantum Design Inc.) and a vibrating sample magnetometer (PPMS, Quantum Design Inc.). Magnetization curves, *M-H* curves were measured at 10 K for the applied field directions perpendicular and parallel to the film. The applied field direction was altered to identify the magnetic easy direction. The temperature dependence of magnetization, *M-T* curves were also measured to evaluate the Curie temperature T_C. To measure the *M-T* curves, the sample was cooled from 300 K to 10 K under the magnetic field of +2 T applied to the direction perpendicular to the film plane. The field was removed after stabilizing temperature at 10 K. The magnetization was measured upon heating the sample from 10 K to 300 K. The T_C value was defined as the temperature at which the magnetization becomes zero. Soft X-ray absorption spectrum (XAS) and soft X-ray magnetic circular dichroism (XMCD) were measured at 80 K. The left- and right-circularly polarized X-ray was irradiated on the sample with the incidence angle 10° from the surface normal. The helicity of the incident X-ray was periodically switched with 1 Hz using the twin-helical undulator [45]. The photon energy was around the Cr $L_{2,3}$ edges. The absorption intensity was measured by the total electron yield (TEY) method with the applied voltage of −36 V. During the measurements, the magnetic field of 1.9 T was applied to the direction perpendicular to the film. XAS and XMCD measurements were done at BL25SU, SPring-8 synchrotron facility. The TEY method is surface-sensitive, $\propto \exp(-t/\lambda)$ (*t* is the distance from the surface and λ is the decay length). Since the decay length at the Cr $L_{2,3}$ edge is reported to be about 0.9 nm [46], these measurements detect the signal from Cr in the vicinity of the surface.

The film structure was analyzed by means of a reflection high-energy electron diffraction (RHEED), an X-ray diffraction (XRD), an X-ray absorption near edge structure (XANES), an extended X-ray absorption fine structure (EXAFS), and a scanning transmission electron microscopy (STEM). The RHEED observations were done *in-situ* for the surface of the $(Cr_{1-x}Al_x)_2O_3$ films. The observations were carried out in the different ultra-high vacuum chamber directly connected with the deposition chamber via the gate valve so that the sample was not exposed to air for the RHEED observations. The acceleration voltage of the electron was 25 kV, and the emission current was typically 50 μA. The XRD measurements were done using the conventional XRD measurement system (RIGAKU Ltd., Smart Lab.) with the Cu K_α irradiation monochromatized using the Ge 220 diffraction. The acceleration voltage and the emission current for the X-ray source was 45 kV and 200 mA, respectively. The lattice parameters, *a* and *c*, were evaluated for the $(Cr_{1-x}Al_x)_2O_3$(0001) films based on the $2\theta/\omega$ profile with the scattering vector *q* along [0001], and the $2\theta_\chi/\phi$ profile with q // $[10\bar{1}0]$, respectively. XANES and EXAFS measurements were measured at the Cr *K* edge. Measurements were done at BL01B1, SPring-8 synchrotron facility. The Athena and

Artemis software [47] were used for the analysis of EXAFS data. The X-ray was irradiated with the incident angle of 80° from the surface normal. The absorption signal was collected by the fluorescence method which detects the signal from the whole film. STEM images were obtained using the JEM ARM200F transmission electron microscope (JEOL Ltd.) operated at 200 kV. The STEM images were collected with the angular dark-field (ADF) imaging method. All structural characterizations were done at room temperature.

3. Results and discussions

3.1. Induction of spontaneous magnetization by Al doping

Figs. 2(a)−2(e) show the magnetization curves measured at 10 K for $x = 0.00 – 0.26$. The film with $x = 0.00$, e.g., the pure Cr_2O_3, does not show the significant magnetization within the magnetic field range, ±2 T due to the antiferromagnetism (Fig. 2(a)). The *M-H* curves for the films with $x = 0.04$, 0.18 and 0.21 show the hysteresis, indicating that the films have the ferro/ferrimagnetic ordering (Figs. 2(b)−2(d)). The M_S values increases from 25 kA/m to 110 kA/m with increasing x from 0.04 to 0.21. The magnitude of M_S is lower than M_S for the typical ferromagnets, e.g., 1735 kA/m for Fe, 1446 kA/m for Co and 508 kA/m for Ni [48]. If the Cr moments were fully aligned in the $(Al_{0.21}Cr_{0.79})_2O_3$ film, the M_S value should be about 770 kA/m using the magnitude of Cr^{3+} moment in Cr_2O_3, 2.48 μ_B [49]. This value is about 6-times higher than the experimentally obtained M_S, 134 kA/m, suggesting the ferrimagnetic ordering in our films. The shape of the *M-H* curves is rectangular for the applied field direction perpendicular to the film, whereas it is a S-shape for the in-plane direction; The films show the perpendicular magnetic anisotropy (PMA). The low M_S helps to obtain the PMA in the 200-nm thick film due to the low demagnetizing field. The M_S value decreases to 11 kA/m for the film with $x = 0.26$ while the PMA is maintained (Fig. 2(e)). Fig. 2(f) plots the M_S at 10 K as a function of x. M_S monotonically increases with increasing x up to $x = 0.21$ and show the abrupt decrease for $x > 0.21$. The first monotonic increase agrees with the previous report [43] although the x value in Ref. 43 was limited below 0.04.

Fallarino et al. reported that the finite magnetization is not highly degraded at $x = 0.3$ [44] although the magnitude of M_S is much lower than our case. They attributed the observed finite magnetization to the boundary magnetization localized at the surface. If the observed magnetization fully relies on the boundary magnetization, the areal saturation magnetization, $M_S{\cdot}t$ would be independent of the thickness. Fig. 3(a) shows the magnetization curves for the $(Al_{0.15}Cr_{0.85})_2O_3(0001)$ films having different thickness ranging from 20 nm to 180 nm. The rectangular hysteresis due to the PMA is maintained for every film. Fig. 3 (b) plots the $M_S{\cdot}t$ value as a function of thickness t. The $M_S{\cdot}t$ value linearly decreases with decreasing thickness. The linear dependence indicates that the spontaneous magnetization relies on the bulk effect. The slope gives the M_S value, 130 kA/m, similar to the value shown in Fig. 2 (f). The difference from the report by Fallarino *et al.* [44] would be attributed to the fabrication process. They prepared the Al-doped Cr_2O_3 films by the high-temperature annealing for the amorphous film. Since this technique would give rise to the random substitution of Al on the Cr site, the uncompensated moment could be canceled out at the bulk site and only the intrinsic boundary magnetization could survive.

Fig. 4 shows the typical *M-T* curves for the films with $x = 0.04 – 0.26$. The magnetization value at 10 K changes with x in the manner shown in Fig. 2(f). The magnetization shows the monotonic decrease with increasing temperature for every x and becomes zero at the x-dependent

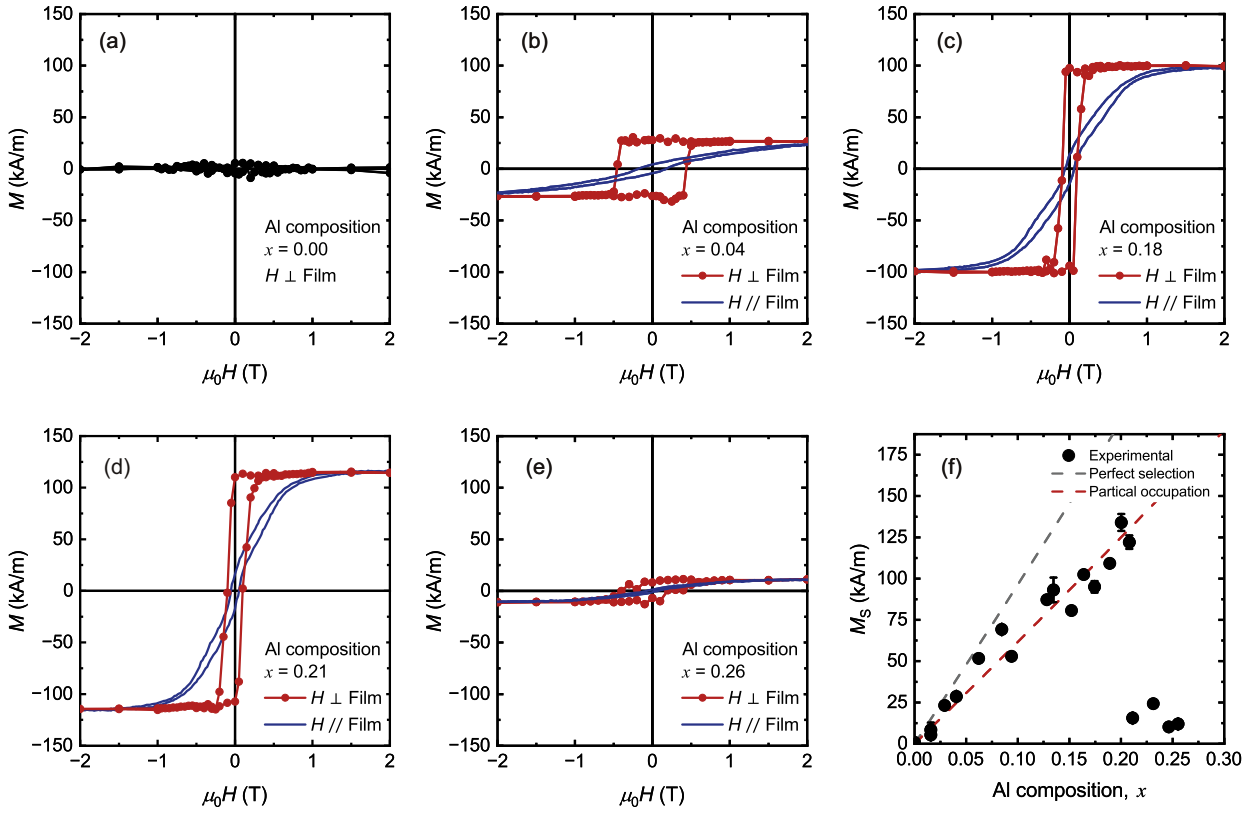

Fig. 2. (a)-(e) Magnetization curves measured at 10 K for the $(Cr_{1-x}Al_x)_2O_3$ films grown on α-$Al_2O_3(0001)$ substrate. Al composition x is (a) 0.00, (b) 0.04, (c) 0.18, (d) 0.21 and (e) 0.26. Red and blue curves represent the curves for the applied magnetic field direction perependicular and parallel to the film plane, respectively (f) Al composition dependence of spontaneous magnetization M_S at 10 K. Gray and red broken lines represent the calculated curves using eq. (1) assuming the perfect selection ($y = 0$) and the partially incorrected occupation ($y = 0.36$), respectively. (see text) Error bar in the M_S value mainly comes from the magnetization measurements and the estimation error of the sample area.

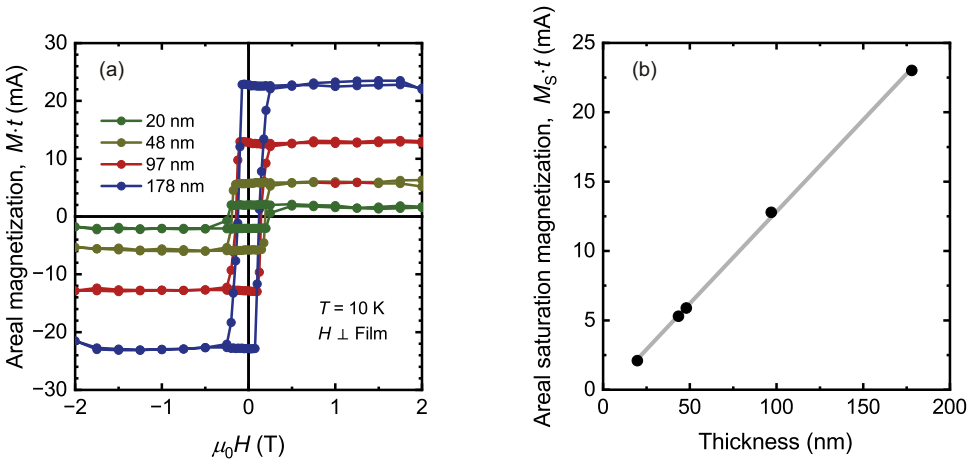

Fig. 3. (a) Magnetization curves of $(Cr_{0.85}Al_{0.15})_2O_3$ film grown on α-Al_2O_3(0001) substrate. The thickness of the film t was varied from 20 nm to 178 nm. The vertical axis is shown as the areal magnetization, $M{\cdot}t$, (b) Thickness dependence of the areal saturation magnetization. The gray line represents the linearly fitted result.

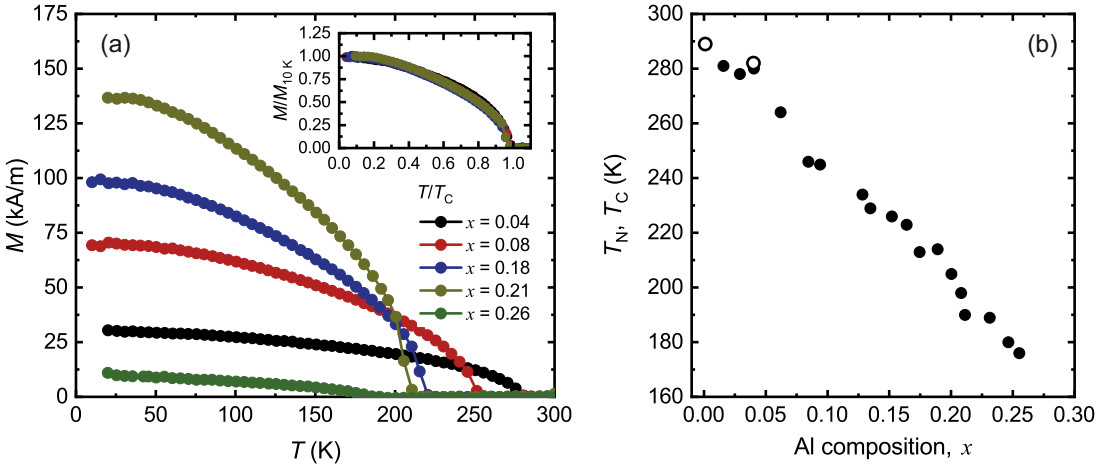

Fig. 4. (a) Temperature dependence of remanent magnetization of $(Cr_{1-x}Al_x)_2O_3$ film grown on α-Al_2O_3(0001) substrate. (b) Al composition dependence of Néel temperature T_N and Curie temperature T_C. Closed circles represent T_C determined by the M-T curve and open circles represent the T_N and T_C determined by the AHE measurements for the films with $x = 0.00$ [47] and 0.04 [48].

Curie temperature, T_C. Fig. 4(b) plots the change in T_C with x. Since the pure Cr_2O_3 does not show the magnetization, the Nèel temperature T_N for this film was determined by the anomalous Hall effect (AHE) measurements [50,51] shown by the open circles. The details of the determination of T_N based on the AHE measurements can be found in Ref. [50]. T_C decreases in the nearly linear fashion with increasing x, which suggests the Al substitution of the Cr site and eventually the decrease in the number of the Cr-Cr coupling. The inset of Fig. 4(a) shows the normalized M-T curves where the magnetization value is normalized by the M_S value at 10 K. A good matching for all curves suggests that the total angular momentum J of individual Cr is unchanged upon the induction of the spontaneous magnetization. One may suppose that the M-T curve can be reproduced by the Brillouin function with a certain J value, e.g., the mean field approximation and it helps the quantitative discussion on the J value. The analysis using the Brillouin function gives the high J value to reproduce the results, above 10, as observed in some ferromagnets [52-54]. The large J does not literally indicate the giant magnetic moment because this analysis is based on the one-body model and some various mechanism such as the spin-wave excitation are not considered. Besides, for the ferrimagnets, the temperature dependence M_S of each sublattice gives the complex temperature dependence of the total M_S [55]. Instead, we evaluate the magnetic moment per Cr by use of the XMCD for some films showing the spontaneous magnetization. For the XMCD measurements, the Pt(2 nm)/$(Cr_{1-x}Al_x)_2O_3$ bilayer was used to ensure the surface conductivity to allow the TEY method. We confirmed that these films showed the similar magnetic properties to the mainly used films. Fig. 5(a) shows the XAS around the Cr $L_{2,3}$ edges for the films with $x = 0.00$ and 0.21. The latter film has the high Al composition and show the high M_S (~125 kA/m at 10 K). The shape of XAS is similar to that for the pure Cr_2O_3 [56] indicating that the valence state of Cr is maintained, e.g., Cr^{3+}. This is reasonable because the valence state of Cr and Al in the thermodynamically equilibrium oxide are both trivalent, and the Al substation does not alter the valence state of Cr. Fig. 5(b) shows the XMCD spectra for the film with $x = 0.00 – 0.21$.The film with $x = 0.00$, the pure Cr_2O_3 does not show the appreciable XMCD signal due to the AFM nature whereas the sizable XMCD intensity is observed for the films with $x = 0.02 – 0.21$, indicating the presence of the uncompensated Cr moment. The shape of XMCD spectra is similar to the previous reports for the pure Cr_2O_3 [57,58]. Besides, the spectrum shape is common to every x except for $x = 0.00$, suggesting that the ligand field on Cr^{3+} is unchanged upon the Al substitution. The magnitude of the XMCD signal increases with increasing x, accompanied with the increase of the M_S value shown in Fig. 2. The sum-rule analysis [59,60] with the spin correction factor [61]

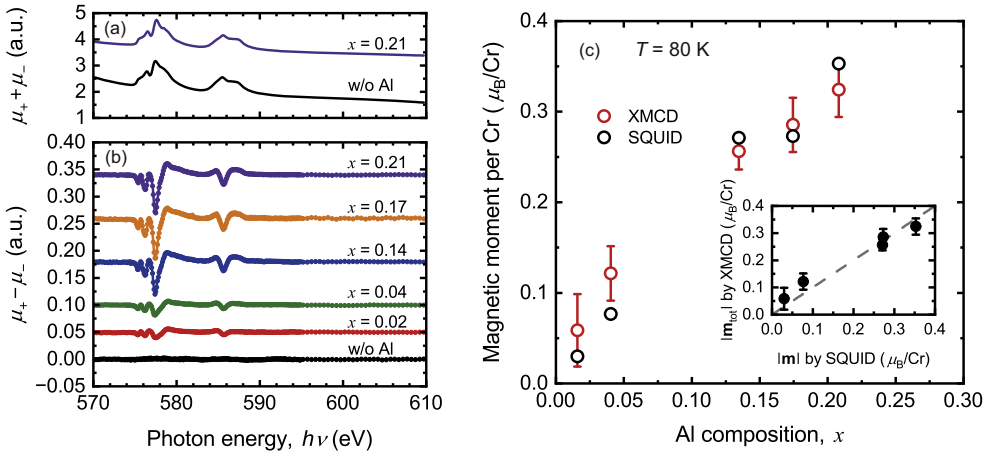

Fig. 5. (a) XAS for the films with $x = 0.00$, e.g., the pure Cr_2O_3 (black) and 0.21 (purple). (b) XMCD spectra measured at $\mu_0 H = 1.9$ T for the films with $x = 0.00$ – 0.21. Measurement temperature was 80 K. (c) x-dependence of magnetic moment per Cr estimated from XMCD (open red circle) and SQUID (open black circle) measurements, respectively. Inset shows the relation between the total magnetic moment per Cr determined by XMCD and SQUID measurements. Error bar in magnetic moment by the XMCD measurements mainly comes from the finite offset when the absorption signals for the opposite circular helicities are subtracted.

gives the effective spin magnetic moment m_{s_eff} and the orbital magnetic moment m_{orb} per Cr^{3+}. For instance, m_{s_eff} and m_{orb} for the film with $x = 0.21$ are 0.31 ± 0.02 μ_B and 0.01 ± 0.02 μ_B, respectively. The total magnetic moment per Cr is about 0.32 μ_B/Cr. Although the TEY method is sensitive to the surface region, the obtained value is significantly lower than the value assuming that the induced M_S is fully localized at the surface, discussed above. Fig. 5(c) plots the total magnetic moment, $m_{tot} = m_{s\_eff} + m_{orb}$ and the magnetic moment per Cr determined by the SQUID measurements as a function of Al composition. The magnetic moments estimated from two distinct techniques show the good matching. These results indicate that the induced finite magnetization is relevant to the amount of the uncompensated moment and that the uncompensated moment is distributed in the whole film. Besides, since the XMCD is element-specific and the SQUID detects the total magnetic moment in the whole film, the good matching indicates that the induced spontaneous magnetization fully relies on Cr. The absence of the magnetic moments in Al^{3+} and O^{2-} is simply anticipated from the outermost shell of these two species; the outermost shell of these elements is $(2p)^6$, a closed shell giving the zero magnetic moment. The valence state of Al was confirmed by the XAS at the Al K edge, and it is discussed in the supplementary information.

3.2. *Relationship between the induction of spontaneous magnetization and the crystal formation*

We identify the reason for the steep decrease in M_S for $x > 0.21$ shown in Fig. 2(f) in association with the change in the crystalline quality of the film. Fig. 6(a)–(f) show the $[11\bar{2}0]_{substrate}$-azimuthal RHEED images for the surface of the $(Cr_{1-x}Al_x)_2O_3$ film with $x = 0.00$ – 0.23. For x below 0.19 (Fig. 6(a)–(e)), the streaks with the elongated spots are observed showing the crystal formation. The observed patterns are indexed by the corundum (0001) with the twin boundary along $[11\bar{2}0]$. In contrast, no diffraction spots or streaks are observed in the RHEED pattern for the film with $x = 0.23$ but the diffuse pattern is obtained. The diffuse pattern indicates that the film is amorphous, or the crystallite size is much smaller than the coherence length of the electron beam. Fig. 7(a) and (b) shows the XRD profiles, $2\theta/\omega$ and $2\theta_\chi/\phi$ profiles for the films with various x. The diffraction peaks nearby Cr_2O_3 0006 and Cr_2O_3 0001$\underline{2}$ in the $2\theta/\omega$ profiles, and those nearby the Cr_2O_3 $30\bar{3}0$ in the $2\theta_\chi/\phi$ profiles are observed in agreement with the RHEED pattern. The diffraction peak position shifts to the high angle with increasing x, indicating the shrink of both a- and c-axis lengths (see also Fig. 7(c) and (d) below). For $x > 0.23$, the diffraction intensity decreases due to the degradation of the crystal formation. It is notable that the steep decrease in M_S (Fig. 2(f)) is associated with the degradation of the XRD profile, and thus, the crystal formation. The weak but finite diffraction in the $2\theta/$

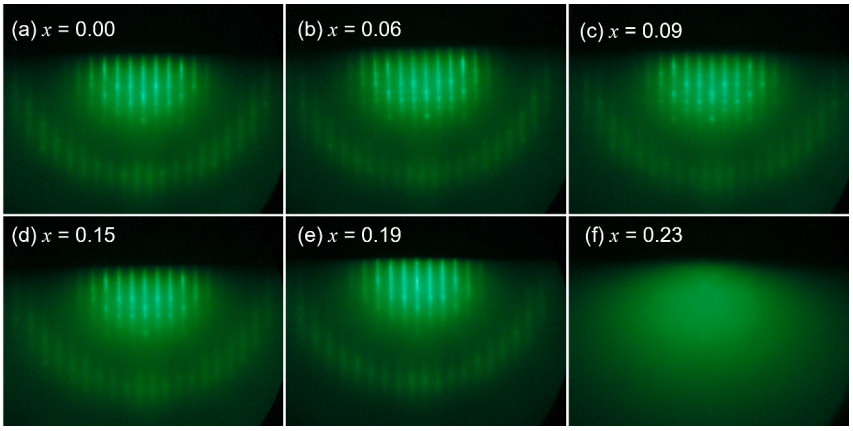

Fig. 6. $[11\bar{2}0]_{substrate}$-azimuthal RHEED images of $(Cr_{1-x}Al_x)_2O_3$ film grown on α-Al_2O_3(0001) substrate. Al composition x is (a) 0.00, (b) 0.06, (c) 0.09, (d) 0.15, (e) 0.19 and (f) 0.23.

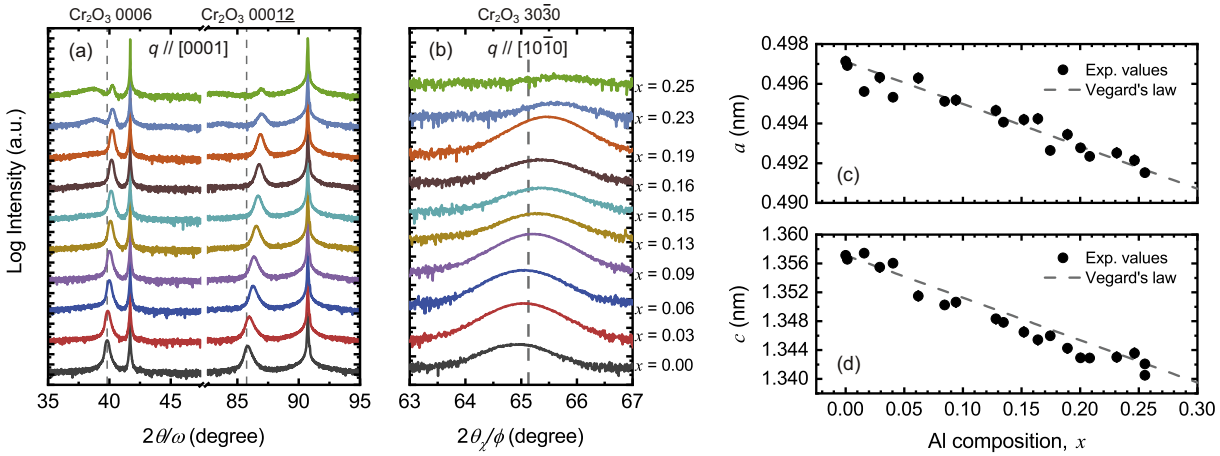

Fig. 7. (a) Out-of-plane ($2\theta/\omega$) and (b) in-plane ($2\theta_\chi/\phi$) XRD profiles of $(Cr_{1-x}Al_x)_2O_3$ film grown on α-Al_2O_3(0001) substrate. Scattering vector q is parallel to (a) [0001] and (b) [10$\bar{1}$0] of substrate, respectively. Al composition dependence of lattice parameter, (c) a and (d) c.

ω profiles are observed for $x = 0.23$ and 0.25 due to the partial crystallization beneath the surface, which would occur during the high temperature growth, 773 K. The broad peak around $2\theta/\omega = 38°$ appear for these films suggesting the formation of the amorphous, which agrees with the diffuse RHEED patterns. The degradation of the crystal formation in the x regime above 0.21 is probably because the crystallization temperature of Al_2O_3 is much higher than Cr_2O_3 and 773 K is not sufficient to crystallize the film with the high x. Fig. 7(c) and (d) show the lattice parameters, a and c as a function of x, respectively. a and c almost linearly decrease with increasing x. The linear decreases in a and c agree with the previous report for the Cr_2O_3-Al_2O_3 solid solution [62, 63]. The slopes of the a- and c-x relationships well matches with the simple interpolation using the lattice parameters of the bulk Al_2O_3 [62-64].

Fig. 8(a) shows the XANES spectra around the Cr K edge. The photon energy at the absorption edge is 6.003 keV, in agreement with the reported value for the Cr_2O_3 [65]. The edge energy is maintained for every film indicating the valence state of Cr is maintained in Cr^{3+} upon the Al substitution in agreement with the above results. Fig. 8(b) shows the radial structure function obtained by Fourier transform of k^3-weighted

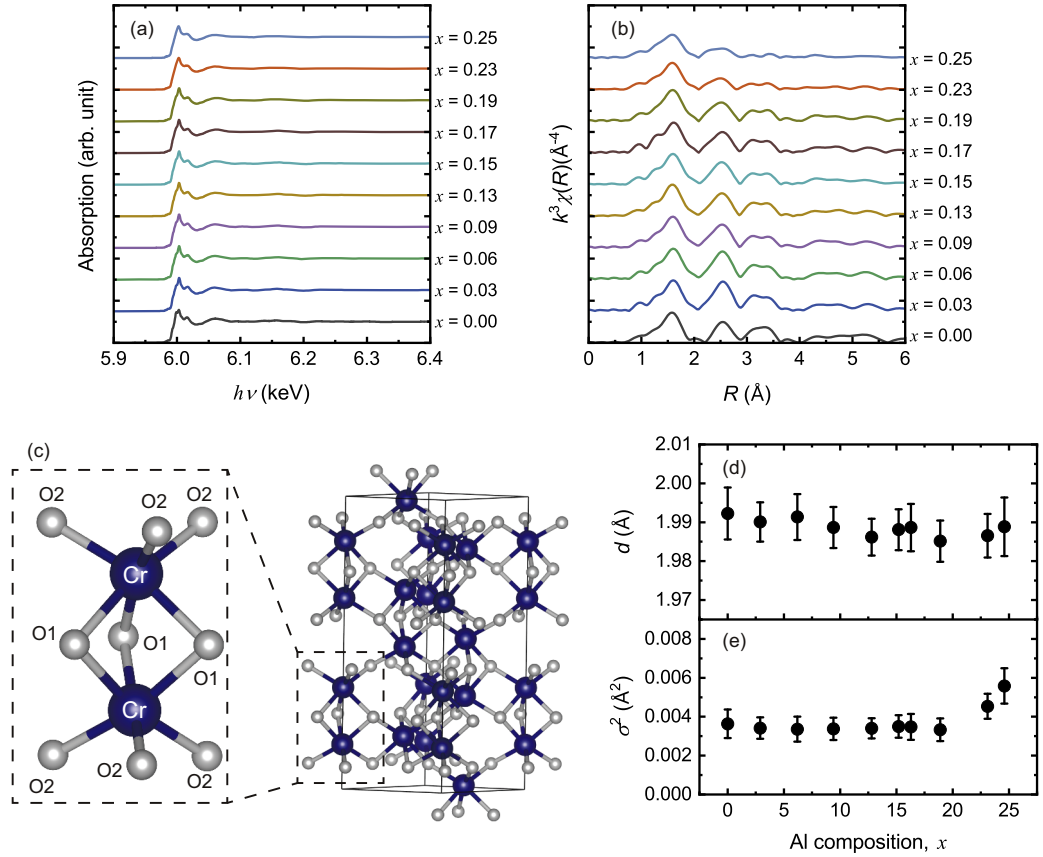

Fig. 8. (a) X-ray absorption spectra and (b) radial structure function around the Cr K edge. (c) Schematic drawing of the crystal structure of Cr_2O_3. Al composition dependence of (d) interatomic distance and (e) Debye-Waller factor for Cr–nearest neighbor O bonding shown in (c). (c) is drawn by VESTA. Error bars in d ad σ^2 mainly come from the fitting error using Artemis/Athena software [47].

EXAFS spectra, $k^3\chi(R)$. Although the overall shape of the EXAFS spectra is maintained for every x, the amplitude of $k^3\chi(R)$ decreases for $x > 0.23$. In the corundum structure, there are two types of the Cr-O bonds, e,g., Cr-O1 and Cr-O2 as shown in Fig. 8(c). Since the bond length of these two bonds are very close, e.g., 2.0132 Å and 1.9644 Å for Cr-O1 and Cr-O2, respectively, it was difficult to distinguish in the analysis with a sufficient accuracy. We treated O1 and O2 as the type O with the six coordination as treated in the previous reports [66]. In the analysis, we evaluated the mean Cr-O bond length d and the Debye-Waller factor σ^2 relevant to the degradation of the crystal formation. On the evaluation, the value of amplitude reduction factor, S_0^2 and the parameter E_0 was determined from the pure Cr_2O_3 as 0.86 and 2.23 eV, respectively, and kept same for all fittings. The k-range for the Fourier transformation was 3 – 14 $Å^{-1}$ and the R range for the fitting was 1 – 2 Å. Fig. 8(d) and (e) plot the d and σ^2 values as a function of x, respectively. The d value shows the slight decrease or is almost constant with increasing x, which implies that the local environment of Cr is robust against the Al doping. The σ^2 value, a measure of the disorder around the target element, is almost constant at 0.0033 for $x < 0.19$ whereas it increases for $x > 0.23$. The increase of σ^2 is also consistent with the degradation of the crystal formation for $x > 0.23$, i.e., the influence of the amorphous phase [67], accompanying with the decrease of M_S.

3.3. Growth-associated mechanism of the spontaneous magnetization

Prior to get into the mechanism of the spontaneous magnetization, we shortly summarize the above results shown in Sections 3.1 and 3.2: (1) The magnitude of M_S increases with increasing x. The induction of the spontaneous magnetization is highly associated with the crystallization of the film. (2) In the crystallized film, the crystal structure is maintained. The lattice parameters show the monotonic decrease with increasing x, and the valence state of Al was trivalent (see supplementary information), suggesting that Al substitutes the Cr site. Upon substituting Cr with Al and consequently inducing the spontaneous magnetization, the valence state and the ligand field of Cr^{3+} are unchanged.

If the Al substitutes the Cr site randomly as in the case of the Cr_2O_3-Al_2O_3 solid solution, the number of magnetic moments having up and down orientation is same, and the numerical imbalance of the opposite magnetic moments is still zero. Eventually, the spontaneous magnetization is not induced. Indeed, the Al 5at% doped Cr_2O_3 sintered powder does show no appreciable magnetization (supplementary information). Therefore, we suppose the mechanism to induce the spontaneous magnetization to meet the above experimental results: the sublattice-selective substitution of Al. Fig. 9 shows the crystal structure of Cr_2O_3 with the magnetic moments [68]. The magnetic moments align up-down-up-down... along the c-axis. When Al substitutes selectively "down" sites, the upward magnetic moments numerically superior giving rise to the finite spontaneous magnetization. However, there is no such ordered phase in the Al_2O_3–Cr_2O_3 equilibrium phase diagram [69]. Besides, the annealing for the amorphous or the sintering for the mixed powder would yield the random substitution as Refs. [62] and [63] and Supplementary Fig. S2 suggested. Therefore, some kind of special substitution process should be involved to form the above phase. According to the crystal structure, the stacking structure along the c-axis is Cr^{3+} (sublattice 1, upward magnetic moment)–O^{2-}–Cr^{3+} (sublattice 2, downward magnetic moment)–O^{2-}... Since the local environments of Cr^{3+} on the sublattices 1 and 2 are distinct at the topmost surface, the occupation energy of Al could be different for each sublattice and the sublattice-selective occupation is basically possible at the topmost surface. The site-dependent occupation energy in the vicinity of the topmost surface in the mixed oxide with corundum structure is theoretically predicted [70], and the similar mechanism has been speculated for the Al and Ir-doped Cr_2O_3(0001) thin film by Nozaki *et al.* [43]. However, such ordered phase has not been identified by the structural investigation. The difficulty to identify such phase is partly due to the unchanging extinction rule for the X-ray diffraction upon the sublattice-selective substitution (for details, see supplementary materials). We approach this issue by altering the growth direction taking advantage of the epitaxial growth. As shown in Fig. 9(a), the stacking structure normal to $(01\bar{1}2)$ is also Cr^{3+} (sublattice 1)–O^{2-}–Cr^{3+} (sublattice 2) although the magnetic moments tilt from the plane normal. The similar growth mechanism and the induction of the spontaneous magnetization are expected. In contrast, when we employ the $(11\bar{2}0)$ growth wherein the stacking structure normal to the growth direction is Cr^{3+} (sublattices 1 and 2)–O^{2-}– O^{2-}–Cr^{3+} (sublattices 1 and 2) (Fig. 9 (b)), the topmost surface is composed of two sublattices. Since the two sublattices energetically degenerate on this surface, Al would substitute equally in the two sublattices. The numerical imbalance of the magnetic moments does not occur in this case, and the spontaneous magnetization should not be induced.

Fig. 10 shows the RHEED images, XRD profiles and cross-sectional STEM images of the $(Cr_{1-x}Al_x)_2O_3$ films with x ~0.13–0.14 grown on the α-$Al_2O_3(01\bar{1}2)$ and the α-$Al_2O_3(11\bar{2}0)$. For both films, the appearance of the diffraction spots in the RHEED images indicates the formation of the crystal. The diffraction pattern is indexed by the corundum $(01\bar{1}2)$ and $(11\bar{2}0)$, respectively, indicating the epitaxial growth; $(Cr_{1-x}Al_x)_2O_3(01\bar{1}2)$ and $(Cr_{1-x}Al_x)_2O_3(11\bar{2}0)$, respectively (hereafter,

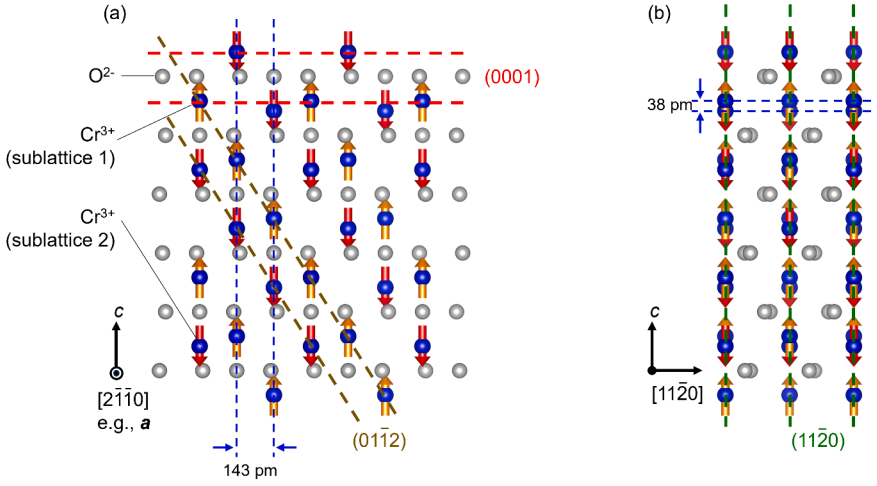

Fig. 9. Schematic drawing of (a) $[2\bar{1}\bar{1}0]$ projected and (b) $[1\bar{1}00]$ projected atom arrangement of Cr_2O_3. Blue and gray circles represent Cr^{3+} and O^{2-}, respectively. Orange and red arrow represents the upward and downward magnetic moments.

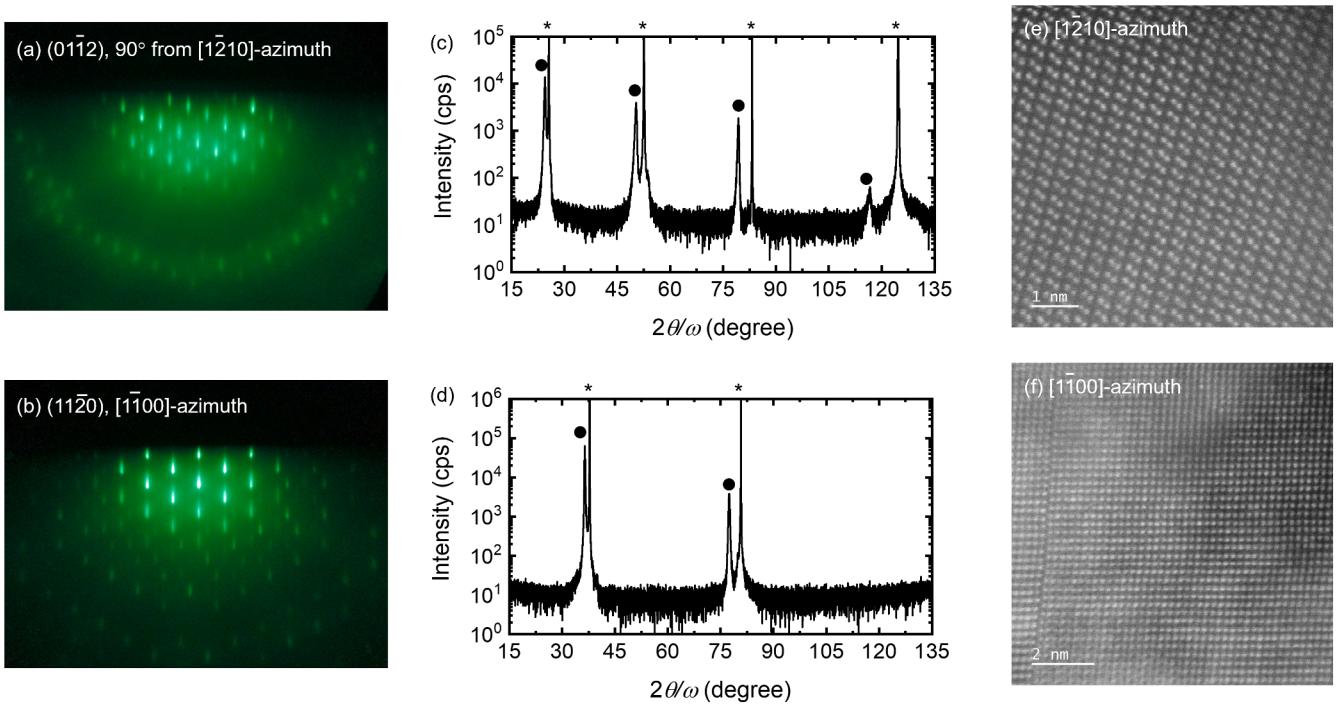

Fig. 10. (a), (b) RHEED image (c), (d) XRD profiles and (e), (f) cross-sectional STEM images for the $(Cr_{1-x}Al_x)_2O_3$ films with $x = 0.13\pm0.01$. (a), (c), (e) are results for the film grown on α-Al_2O_3(01$\bar{1}$2) and (b), (d), (f) are results for the film grown on α-Al_2O_3(11$\bar{2}$0). Closed circles and * reprent the diffraction from the film and the substrate, respectively.

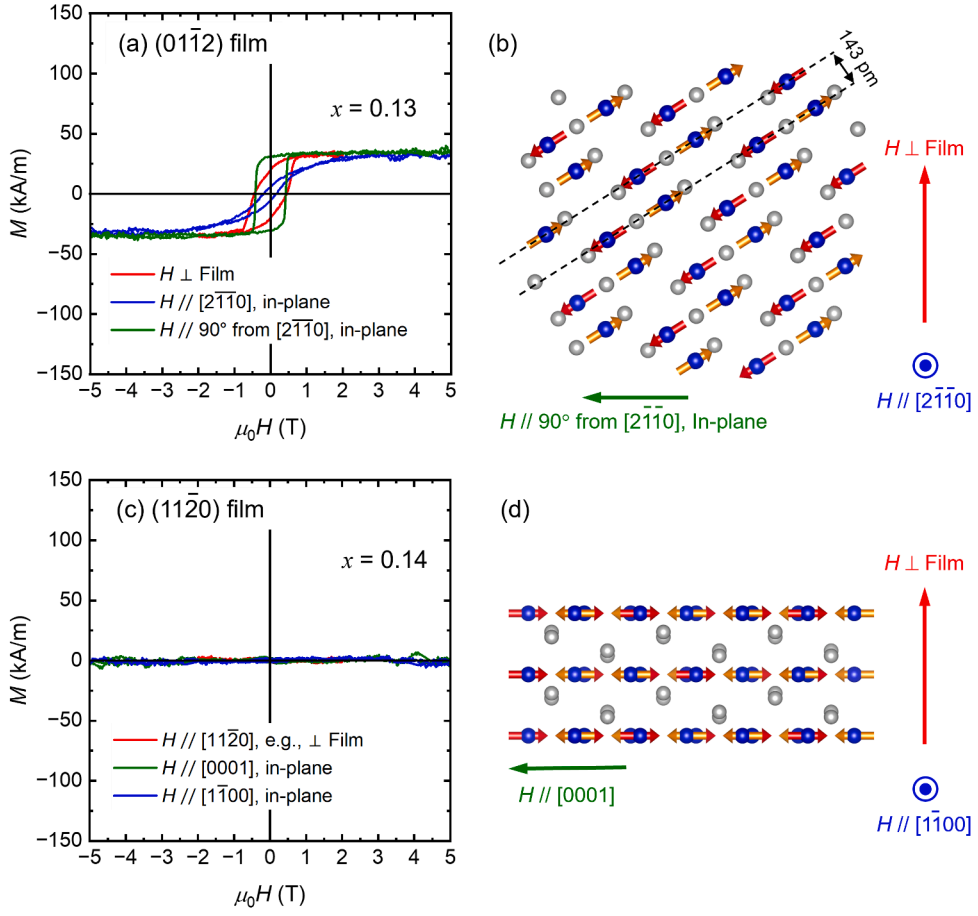

Fig. 11. Magnetization curves measured at 10 K for the $(Cr_{1-x}Al_x)_2O_3$ films with $x = 0.13\pm0.01$. (a) and (b) are results for the film grown on α-Al_2O_3(01$\bar{1}$2) and α-Al_2O_3(11$\bar{2}$0), respectively. Right images on each *M-H* loops represents the schematic drawing of the crystal structure with the applied magnetic field direction.

denoted as *r*-film and *a*-film, respectively). In particular, the RHEED pattern for the *r*-film (Fig. 10(a)) is asymmetric with respect to (00) streak, indicating the formation of the single-crystalline film. In the XRD profiles with q // surface normal (Fig. 10(c) and (d)), the diffraction peaks from the intended planes are only observed.; for the *r*-film, the diffractions from $(Cr_{1-x}Al_x)_2O_3(01\bar{1}2)$, $(02\bar{2}4)$, $(03\bar{3}6)$, and $(04\bar{4}8)$ are observed, and for the *a*-film, the diffractions from $(Cr_{1-x}Al_x)_2O_3(11\bar{2}0)$ and $(22\bar{4}0)$ are observed, except for the diffraction from the substrate (shown by *). Fig. 10(e) and (f) show the cross-sectional STEM images for the *r*- and *a*-films, respectively. In the STEM image for the *r*-film, the tilted dumbbell structure depicted in Fig. 9(a) is resolved indicating that the supposed layered structure by the magnetic sublattice is formed. In contrast, the cross-sectional image (Fig. 10(f)) for the *a*-film shows the simple periodic structure, and the dumbbell structure could not be resolved in the ADF image due to the very close lateral atom position (38pm) on the sublattice as depicted in Fig. 9(b). One may wonder that when the STEM observation with the orthogonal incidence would resolve the dumbbell structure. Although this is the case with the [0001]-azimuth, the dumbbell structure is not formed along this incidence and the magnetic sublattices are not resolved because two magnetic sublattices lie on the same line along [0001]. (see also Fig. 9 and supplementary materials).

Fig. 11 shows the *M-H* curves measured at 10 K for two types of films. The *r*-film shows the hysteresis indicating the emergence of the spontaneous magnetization (Fig. 11(a)). The shape of the *M-H* changes with the applied field direction due to the magnetic anisotropy. For the applied field direction is 90° from $[2\bar{1}\bar{1}0]$ lying on the film plane, the loop is nearly the square, whereas the loop becomes gradual for the applied field direction parallel to $[2\bar{1}\bar{1}0]$. The loops along $[01\bar{1}2]$ is intermediate between two loops. The difference in the loop shape is attributed to the magnetocrystalline anisotropy of Cr_2O_3 with the magnetic easy axis parallel to *c*-axes, [0001] [68]. The green curve for $H \perp [2\bar{1}\bar{1}0]$ lying on the film plane is closest to [0001] among three directions, whereas the blue curve for H // $[2\bar{1}\bar{1}0]$ is farthest from [0001]. This is relevant to the demagnetizing energy much lower than the magnetocrystalline anisotropy energy in consistent with the case of the $(Cr_{1-x}Al_x)_2O_3(0001)$ film (hereafter, denoted as *c*-film) shown in Section 3.1. In contrast, no appreciable magnetization was observed in the *a*-film in any applied field direction (Fig. 11(b)). The absence of the spontaneous magnetization is consistent with the above prediction.

We verify the sublattice-selective substitution by the direct observation using the ADF-STEM.Fig. 12 shows the atomic resolution cross-sectional ADF images, the line profile of contrast and the schematic drawing of the atom arrangement projected from the zone-axis. The clear twin boundary along the vertical direction is observed in the *c*-film (Fig. 12(a)), in agreement with the RHEED observation. In the ADF images, the atom pairs corresponding to the sublattice shown by the dotted square are observed. Cr and Al in the atom pair could be distinguished by the *Z*-contrast, $\propto Z^{\alpha}$ with α (~1 - 2) due to the Rutherford scattering [71-73]. The line profiles (Fig. 12(b) and (c)) in the yellow squares, corresponding to the colored band in Fig. 11(d), show two types of amplitude in the intensity. Besides, the relationship of the bright/dark contrast is same in the different atom pair: blight left and dark right in Fig. 12(b). This relationship of the brightness is reversed in another twin

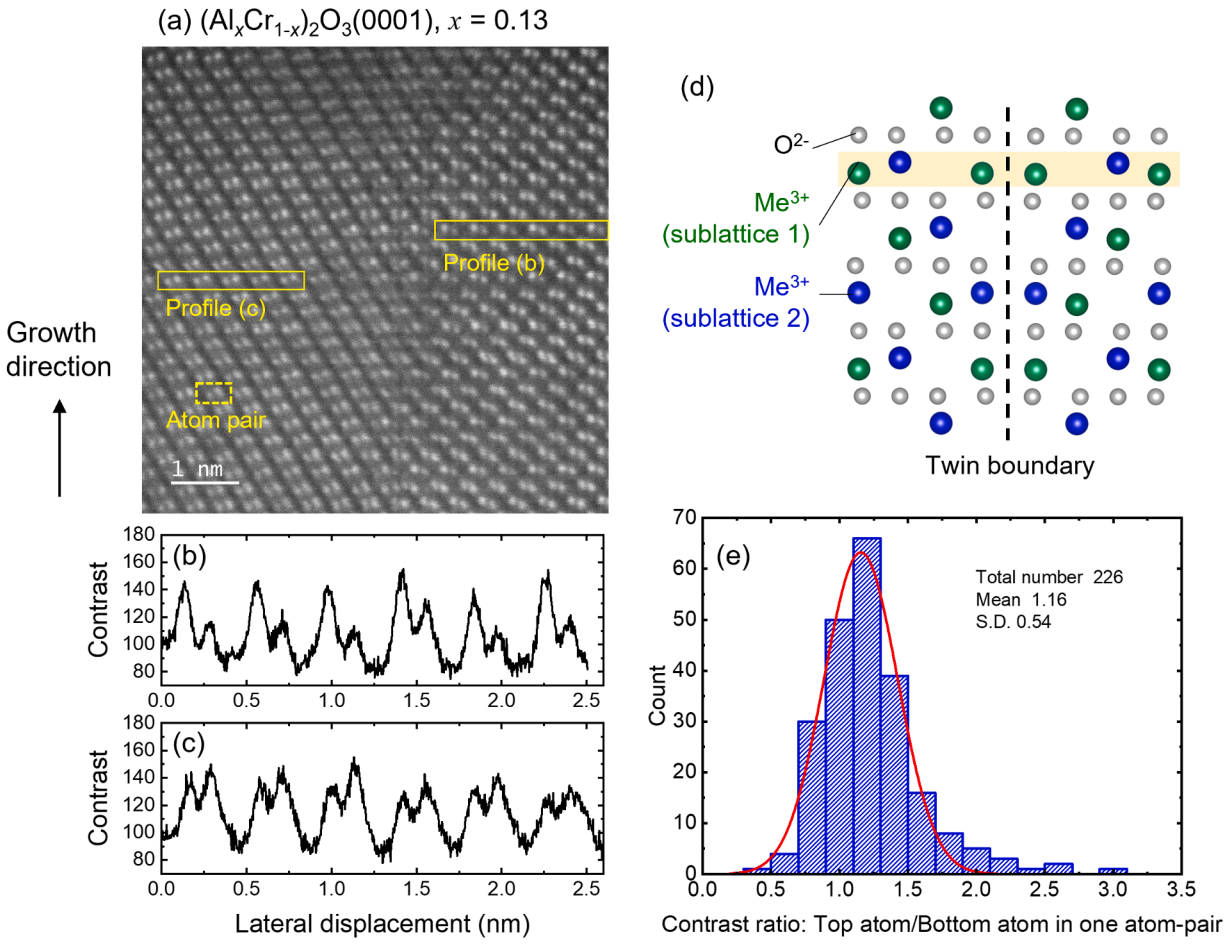

Fig. 12. (a) Cross-sectional STEM images, (b), (c) the line profiles marked in the image, (d) schematic drawing of the projected atom arrangement with spin alignment and (e) histogram of the contrast ratio defined by top-atom/bottom-atom in one atom-pair. The results are for $(Cr_{1-x}Al_x)_2O_3(0001)$ films with $x = 0.13$. The red line in (e) represents the fitted results assuming the normal distribution.

domain; dark left and blight light in Fig. 12(c). For both twin domains, the lower atom in the atom pair is selectively substituted by Al. To further evaluate the site-selective substitution of Al, we analyzed the contrast ratio for over 200 atom pairs. Fig. 12(e) shows the histogram of the contrast ratio. The contrast ratio is defined as the top/bottom atoms in one atom pair. The mean value of the constant ratio is 1.16. The deviation form 1 is of particularly important because it indicates that the different species selectively occupy the one-side in the atom-pair.; In our case, the heavy atom, e.g., Cr selectively occupies the top site.

One may assume that the quantitative analysis of the *Z*-contrast gives the average composition on each site and resultantly, the imperfection of the sublattice-selective substitution which is associated with the M_S value. However, the thickness effect on α hampers the quantitative analysis of the *Z*-contrast [71]. (see also Supplementary materials) Alternatively, we analyze the incorrect occupation of Al by analyzing the *x*-dependence of M_S shown in Fig. 2(f). We suppose that the nonmagnetic Al preferentially occupies one magnetic sublattice and the part of the population occupies another magnetic sublattice. Denoting the incorrect occupation ratio of Al as *y*, $y = 0$ (a perfect selection) and 1(a random substitution), the induced saturation magnetization is derived as

$$M_S(x) = \frac{N \cdot m_{Cr}}{V(x)} x(1-y) \quad (1)$$

N is the number of Cr atom in the unit cell, m_{Cr} is the magnetic moment per Cr, 2.48 μ_B [49], x (= 0 – 0.5) is the Al composition, and $V(x)$ is the unit cell volume. Taking a hexagonal unit cell, $N = 12$, $V(x)$ is calculated using the lattice parameters which depend on x by the Vegard's law (see Fig. 7(c) and (d)). Assuming the perfect selection of the magnetic sublattice, i.e., $y = 0$, the calculated curve (the gray dotted line in Fig. 2(f)) represents the trend of the M_S value, whereas the experimental value shows the lower deviation which is significant for $x > 0.1$. Assuming that y is independent of x, eq. (2) with $y = 0.36$ well reproduces the experimental M_S-x relationship (the red dotted line in Fig. 2(f)). The incorrect occupation can occur in the high temperature growth, for example, by the Boltzmann distribution of the occupation energy on each site.

4. Summary

We investigated the Al-doped Cr_2O_3 thin film exhibiting the spontaneous magnetization, as the class of ME ferrimagnetic insulator. The $(Cr_{1-x}Al_x)_2O_3$ films grown on α-Al_2O_3(0001) substrates showed the spontaneous magnetization. The magnitude of M_S increased linearly with increasing x below 0.21. The *M*–*T* curve, the T_C–x relationship, the XAS/XMCD spectra and the averaged magnetic moment per Cr suggests that the ligand field on Cr is maintained upon inducing the spontaneous magnetization. The M_S value abruptly decreases for $x > 0.21$, which is associated with the degradation of the crystal formation. The lattice parameters, the mean Cr-O bond length suggested that the Al substituted the Cr site. Since the random substation of Al does not give rise to the finite spontaneous magnetization, the special substitution mechanism such as the magnetic sublattice-selective substitution would be involved in the growth process. We prove this mechanism by using the $(Cr_{1-x}Al_x)_2O_3(01\bar{1}2)$ and $(Cr_{1-x}Al_x)_2O_3(11\bar{2}0)$ films; the former showed the spontaneous magnetization whereas the latter did not. The layer-by-layer stacking structure by the magnetic sublattice would generate the different occupation energy of Al at the topmost surface, which would yield the sublattice-selective substitution during the thin film growth. We observed this specific substation directly by the STEM observations.

Our investigation demonstrated that the specific substitution occurred associated with the thin film growth process along the proper growth direction. The selective substitution is relevant to the magnetic sublattice, yielded the numerical imbalance of the magnetic moments, and consequently, induced the finite spontaneous magnetization in the AFM insulator. The demonstrated fabrication process is distinct from the process based on the metallurgical approach based on the thermal treatment and will be applicable in various oxide materials, which expands a material choice of the ME insulator as well as the oxide ferrimagnetic materials.

Data availability

The data that support the finding of this study are available from the corresponding author upon reasonable request.

CRediT authorship contribution statement

Tatsuo Tada: Data curation, Formal analysis, Writing – review & editing. **Hiroki Sakurai:** Data curation, Formal analysis, Writing – review & editing. **Kentaro Toyoki:** Formal analysis, Investigation, Writing – review & editing. **Satoshi Ichikawa:** Data curation, Formal analysis, Methodology, Writing – review & editing. **Toshiaki Ina:** Data curation, Methodology, Writing – review & editing. **Noriaki Kishida:** Data curation, Writing – review & editing. **Yoshinori Kotani:** Data curation, Methodology, Writing – review & editing. **Masashi Nakamoto:** Data curation, Methodology, Writing – review & editing. **Kota Mori:** Data curation, Writing – review & editing. **Ryoichi Nakatani:** Supervision, Writing – review & editing. **Yu Shiratsuchi:** Conceptualization, Data curation, Formal analysis, Funding acquisition, Methodology, Supervision, Writing – original draft, Writing – review & editing.

Declaration of competing interest

The authors declare no non-financial interest but declare a competing financial interest. A patent application related to this research has been filed.

Acknowledgements

XAS and XMCD measurements were carried out at BL25SU, and XANES and EXAFS measurements were carried out at BL01B1, SPring-8, Japan with the approval of JASRI, Project Nos. 2021B1206 and 2021B1207. This work is partly supported by JSPS KAKENHI (Grant Nos. 22H01757, 22K18903) and Iketani Science and Technology Foundation (Project No. 0341023-A).

Supplementary materials

Supplementary material associated with this article can be found, in the online version, at doi:10.1016/j.actamat.2024.120027.

References

[1] C.D. Stanciu, A.V. Kimel, F. Hansteen, A. Tsukamoto, A. Itoh, A. Kirilyuk, T. Rasing, Phys. Rev. B 73 (2006), 220402(R).
[2] I. Radu, K. Vahaplar, C. Stamm, T. Kachel, N. Pontius, H.A. Dürr, T.A. Ostler, J. Barker, R.F.L. Evans, R.W. Chantrell, A. Tsukamoto, A. Itoh, A. Kirilyuk, Th. Rasing, A.V. Kimel, Nature 472 (2011) 205.
[3] T. Kampfrath, A. Sell, G. Klatt, A. Pashkin, S. Mährlein, T. Dekorsy, M. Wolf, M. Fiebig, A. Leitenstofer, R. Huber, Nat Photon. 5 (2011) 31.
[4] J.H. Mentink, J. Hellsvik, D.V. Afanasiev, B.A. Ivanov, A. Kirilyuk, O. Eriksson, M. T. Katsnelson, T. Rasing, Phys. Rev. Lett. 108 (2012) 057202.
[5] S. Baiel, M. Hohenkeutner, T. Kampfrath, A.K. Zvezdin, A.V. Kimel, R. Huber, R. V. Mikhaylovskiy, Nat Photonics 10 (2016) 715.
[6] S. Mondal, Y. Lin, D. Polley, C. Su, A. Zettl, S. Salahuddin, J. Bonkor, ACS Nano 16 (2022) 9020.
[7] S. Funada, Y. Ishikawa, M. Kimata, K. Hayashi, T. Sano, K. Sugi, Y. Fujii, S. Mitsudo, Y. Shiota, T. Ono, T. Moriyama, Phys. Rev. Appl. 19 (2023) L031003.
[8] S.K. Kim, G.S.D. Beach, K.J. Lee, T. Ono, T. Rasing, H. Yang, Nature Mater 21 (2022) 24.
[9] S. Woo, K.M. Song, X. Zhang, Y. Zhou, M. Ezawa, X. Liu, S. Finizio, J. Raabe, N. J. Lee, S.I. Kim, S.Y. Park, Y. Kim, D.Lee J-Y.Kim, O. Lee, J.W. Choi, B.C. Min, H. C. Koo, J. Chang, Nature Comm 9 (2018) 959.
[10] C.E. Graves, A. Reid, T. Wang, B. Wu, S. de Jong, K. Vahaplar, I. Radu, D. P. Bernstein, M. Messershcmidt, L. Müller, R. Coffee, M. Bintna, S.W. Epp,

R. Hartmann, N. Kimmel, G. Hauser, A. Hartmann, Holl P, H. Gorke, J.H. Mentink, A. Tsukamoto, A. Fognini, J.J. Turner, W.F. Schlotter, D. Rolles, H. Soltau, L. Stüder, Y. Acremann, A.V. Kimel, A. Kirilyuk, Th. Rasing, J. Stöhr, A.O. Schrez, H.A. Dürr, Nature Mater 12 (2013) 293.
[11] L. Bainsla, A. Kumar, A.A. Awad, C. Wang, M. Zahedinejad, N. Behera, H. Fulara, R. Khymyn, A. Houshang, J. Weissenrieder, J. Åkerman, Adv. Funct. Mater. 32 (2022) 2111693.
[12] H. Wu, S. Turan, Q. Pan, C.Y. Yang, G. Wu, S.A. Razavi, B. Daai, N.T. Yardimci, Z. Huang, J. Zhang, Y.Y. Chin, H.J. Lin, C.H. Lai, Z. Zhang, M. Jarrahi, K.L. Wang, Phys. Rev. Appl. 18 (2022) 064012.
[13] T. Sumi, T. Senoo, M. Horio, S. El Moussaoui, E. Nakamura, K. Tanaka, A. Tsukamoto, I. Matsuda, Jpn. J. Appl. Phys. 62 (2023) SB8001.
[14] R.C. Bhatt, L.X. Ye, N.C. Huang, T.H. Wu, J. Magn. Magn. Mater. 580 (2023) 170881.
[15] K. Ueda, M. Mann, P.W.P. de Brouwer, D. Bono, G.S.D. Beach, Phys. Rev. B 96 (2017) 064410.
[16] W. Li, J. Yan, M. Tang, S. Lou, Z. Zhang, X.L. Zhang, Q.Y. Jin, Phys. Rev. B 97 (2018) 184432.
[17] Z. Ji, Y. Song, Y. Liu, Y. Zhang, Z. Li, Y. Song, J. Zhang, S. Lou, Z. Zhang, Q. Jin, Appl. Phys. Lett. 123 (2023) 132401.
[18] K.J. Kim, S.K. Kim, Y. Hirata, S.H. Oh, T. Tono, D.H. Kim, T. Okuno, W.S. Ham, S. Kim, G. Go, Y. Tserkovnyak, A. Tsukamoto, T. Moriyama, K.J. Lee, T. Ono, Nature Mater 16 (2017) 1187.
[19] L. Caretta, M. Mann, F. Büttner, K. Ueda, B. Pfau, C.M. Güunther, P. Hassing, A. Churikova, C. Klose, M. Shuneider, D. Engel, C. Marcus, D. Bono, K. Bagschik, S. Eisebitt, G.S.D. Beach, Nat Nanotechnol 13 (2018) 1154.
[20] I.E. Dyzloshinskii, J. Exptl. Theoret. Phys. 37 (1959) 881.
[21] D.N. Astrov, J. Exptl. Thoeret. Phys. 40 (1961) 1035.
[22] G.T. Rado, Phys. Rev. Lett. 6 (1961) 609.
[23] M. Fiebig, J. Phys. D Appl. Phys. 38 (2005) R123.
[24] Y. Shiratsuchi, K. Toyoki, R. Nakatani, J. Phys. Condens. Mater. 33 (2021) 243001.
[25] P. Borisov, A. Hochstrat, X. Chen, W. Kleeman, C. Binek, Phys. Rev. Lett. 94 (2005) 117203.
[26] X. He, Y. Wang, N. Wu, A.N. Caruso, E. Vescovo, K.D. Belashchenko, P.A. Dowen, C. Binek, Nature Mater 9 (2010) 579.
[27] K. Toyoki, Y. Shiratsuchi, T. Nakamura, C. Mitsumata, S. Harimoto, Y. Takechi, T. Nishimura, H. Nomura, R. Nakatani, Appl. Phys. Express 7 (2014) 114201.
[28] T. Ashida, M. Oida, N. Shimomura, T. Nozaki, T. Shibata, M. Sahashi, Appl. Phys. Lett. 104 (2014) 152409.
[29] T. Ashida, M. Oida, N. Shimomura, T. Nozaki, T. Shibata, M. Sahashi, Appl. Phys. Lett. 106 (2015) 132407.
[30] K. Toyoki, Y. Shiratsuchi, A. Kobane, C. Mitsumata, Y. Kotani, T. Nakamura, R. Nakatani, Appl. Phys. Lett. 106 (2015) 162404.
[31] Y. Hui, W. Lin, Q. Xe, S. Chen, X. Miao, J. Chen, J. Phys. D: Appl. Phys. 52 (2019) 24LT03.
[32] K. Toyoki, Y. Shiratsuchi, A. Kobane, S. Harimoto, S. Onoue, H. Nomura, R. Nakatani, J. Appl. Phys. 117 (2015) 17D902.
[33] T.V.A. Nguyen, Y. Shiratsuchi, A. Kobane, S. Yoshida, R. Nakatani, J. Appl. Phys. 122 (2017) 073905.
[34] T.V.A. Nguyen, Y. Shiratsuchi, S. Harimoto, S. Yonemura, T. Shibata, R. Nakatani, J. Appl. Phys. 124 (2018) 233902.
[35] M. Al-Mahdawi, S.P. Pati, Y. Shiokawa, S. Ye, T. Nozaki, M. Sahashi, Phys. Rev. B 95 (2017) 144423.
[36] W. Liu, B. Chen, T. Miao, J. Xie, L. Liu, G. Zhou, H. Qin, J. Hu, J. Magn. Magn. Mater. 491 (2019) 165500.
[37] C. Love, J.E. Beevers, B. Achinuq, R. Fan, K. Matsuzaki, T. Susaki, V.K. Lazarov, S. S. Dhesi, G. van der Laan, S.A. Cavill, Phys. Rev. B 107 (2023) 064414.
[38] V.V. Balashev, K.S. Ermakov, D.A. Tsukabov, A. Yu. Samardak, A.V. Ognev, A. S. Samardak, J. Alloys and Compounds 961 (2023) 170967.
[39] C.Y. Guo, C.H. Wan, M.K. Zhao, K. Wu, Z.R. Yan, J. Feng, H.F. Liu, X.F. Fan, Appl. Phys. Lett. 114 (2019) 192409.
[40] Y. Yang, T. Liu, L. Deng, J. Alloys Compounds 860 (2021) 158235.
[41] K. Fukushima, K. Ueda, N. Moriuchi, T. Kida, M. Hagiwara, J. Matsuno, Appl. Phys. Lett. 121 (2022) 232403.
[42] T. Arima, J. Phys. Soc. Jpn 80 (2011) 052001.
[43] T. Nozaki, M. Al-Mahdawi, Y. Shiokawa, S.P. Pati, S. Ye, K. Kotani, Toyoki K, T. Nakamura, M. Suzuki, S. Yonemura, T. Shibata, M. Sahashi, Phys. Status Solidi RPL 12 (2018) 1800366.
[44] L. Falliano, C. Binek, A. Berger, Phys. Rev. B 91 (2015) 214403.
[45] T. Muro, T. Nakamura, T. Matsushita, H. Kimura, T. Nakatani, T. Hirono, T. Kubo, K. Kobayashi, Y. Saitoh, M. Takeuchi, T. Hara, K. Shirasawa, H. Kitamura, J. Electron Spectrosc, Relat. Phenom. 1101 (2005) 144–147.
[46] B.H. Frazer, et al., Surf. Sci. 537 (2003) 161–167.
[47] B. Ravel, M. Newville, J. Synchrotron Rad. 12 (2005) 537.
[48] R.M. Borzoth, Ferromagnetism, 54, John Wiley and Sons, Inc., New Jersey, 2003, p. 270, 264.
[49] P.J. Brown, et al., J. Phys.: Condens. Matter 14 (2002) 1957.
[50] X. Wang, K. Ujimoto, K. Toyoki, R. Nakatani, Y. Shiratsuchi, Appl. Phys. Lett. 121 (2002) 182402 and supplementary information.
[51] I. Iino, T. Tada, K. Toyoki, R. Nakatani, Y. Shiratsuchi, AIP Adv. 13 (2023) 015035.
[52] Y. Sugita, H. Takahashi, M. Komuro, M. Igarashi, R. Imura, T. Kabme, J. Appl. Phys. 79 (1996) 5576.
[53] N. Inaba, Y. Uesaka, M. Futamoto, IEEE Trans. Magn. 36 (2000) 54.
[54] S. Okamoto, N. Kikuchi, O. Kitakami, T. Miyazaki, Y. Shimada, K. Fukamichi, Phys. Rev. B 66 (2013) 024413.
[55] A.H. Morrish, The Physical Principles of Magnetism, IEEE Press, New York, 2001, pp. 494–501.
[56] Y. Yamazaki, T. Kataoka, V.R. Singh, A. Fujimori, F.H. Chang, D.J. Huang, H.J. Lin, C.T. Chen, K. Ishikawa, Z. Zhang, S. Kuroda, J. Phys.: Condens. Matter 23 (2011) 176002.
[57] K. Ujimoto, H. Sameshima, K. Toyoki, Y. Kotani, T. Moriyama, K. Nakamura, R. Nakatani, Y. Shiratsuchi, Appl. Phys. Lett. 123 (2023) 022407.
[58] T. Moriyama, Y. Shiratsuchi, T. Iino, H. Aono, M. Suzuki, T. Nakamura, Y. Kotani, R. Nakatani, K. Nakamura, T. Ono, Phys. Rev. Appl. 13 (2020) 034052.
[59] B.T. Thole, P. Carra, F. Sette, G. van de Laan, Phys. Rev. Lett. 68 (1992) 1943.
[60] P. Carra, B.T. Thole, M. Altarelli, X. Wang, Phys. Rev. Lett. 70 (1993) 694.
[61] E. Goering, Phil. Mag. 88 (2005) 2895.
[62] P. Zhao, H. Zhao, J. Yu, H. Zhan, H. Gao, Q. Chen, Ceram. Int. 44 (2018) 1356.
[63] R. Jangir, V. Srihari, A. Bhakar, C. Kamal, A.K. Yadav, P.R. Sagdeo, D. Kumar, S. Tripathi, S.N. Jha, T. Ganguli, J. Appl. Phys. 128 (2020) 135703.
[64] J. Graham, J. Phys. Chem. Solids 17 (1960) 18.
[65] E. Groppo, C. Prestipino, F... Cesano, F. Bonino, S. Bordiga, C. Lamberti, P. C. Thüne, J.W. Niemantsverdriet, A. Zecchina, J. Catal. 230 (2005) 98.
[66] T.C. Kasper, P.V. Sushko, M.E. Bowden, S.M. Heald, A. Papadogianni, C. Tschammer, O. Bierwagen, S.A. Chambers, Phys. Rev. B 94 (2016) 155409.
[67] B.K. Teo, H.S. Chen, R. Wang, M.R. Antonio, J. Non crystalline Solids 58 (1983) 249.
[68] M. Tachiki, T. Nagamiya, J. Phys. Soc. Jpn. 13 (1958) 452.
[69] S.S. Kim, T.H. Sandes Jr., J. Am. Ceram. Soc. 84 (2001) 1881.
[70] A.S.M. Jonayat, A. Kramer, L. Bignardi, P. Lacovig, S. Lizzit, A.C.T. van Duin, M. Batzill, M.J. Janik, Phys. Chem. Chem. Phys. 20 (2018) 7073.
[71] P. Hartel, H. Rose, C. Dinges, Ultramicroscopy 63 (1996) 93.
[72] K. Ishizuka, Ultramicroscopy 90 (2002) 71.
[73] M.M.J. Treacy, Microsc. Microanal. 17 (2011) 847.